The Journal of Chemical Physics

RAPID COMMUNICATION | OCTOBER 22 2025

Learning the bulk and interfacial physics of liquid–liquid phase separation with neural density functionals

Silas Robitschko ; Florian Sammüller ; Matthias Schmidt ; Robert Evans

J. Chem. Phys. 163, 161101 (2025)
https://doi.org/10.1063/5.0290261

The Journal of Chemical Physics COMMUNICATION pubs.aip.org/aip/jcp

Learning the bulk and interfacial physics of liquid–liquid phase separation with neural density functionals

Cite as: J. Chem. Phys. 163, 161101 (2025); doi: 10.1063/5.0290261
Submitted: 11 July 2025 • Accepted: 2 October 2025 •
Published Online: 22 October 2025

Silas Robitschko,[1] Florian Sammüller,[1] Matthias Schmidt,[1,a)] and Robert Evans[2]

AFFILIATIONS

[1] Theoretische Physik II, Physikalisches Institut, Universität Bayreuth, D-95447 Bayreuth, Germany
[2] H. H. Wills Physics Laboratory, University of Bristol, Royal Fort, Bristol BS8 1TL, United Kingdom

[a)] **Author to whom correspondence should be addressed:** Matthias.Schmidt@uni-bayreuth.de

ABSTRACT

We use simulation-based supervised machine learning and classical density functional theory to investigate bulk and interfacial phenomena associated with phase coexistence in binary mixtures. For a prototypical symmetrical Lennard-Jones mixture, our trained neural density functional yields accurate liquid–liquid and liquid–vapor binodals together with predictions for the variation of the associated interfacial tensions across the entire fluid phase diagram. From the latter, we determine the contact angles at fluid–fluid interfaces along the line of triple-phase coexistence and confirm that there can be no wetting transition in this symmetrical mixture.

Making accurate predictions for the phase behavior of complex systems remains a major computational challenge despite the availability of a wide variety of flexible simulation methodology.[1] The particular phenomenon of liquid–liquid phase separation occurs across a broad spectrum of substances, from mixtures of simple (rare gas) liquids[2] to models of water[3] and ouzo.[4,5] Moreover, liquid–liquid phase separation is argued to be a possible structure formation mechanism in biological cells,[6] where much theoretical work has been carried out on the basis of the Flory–Huggins model. Studying the emergence of phase transitions provides fertile ground for the development of machine-learning strategies[7–9] and for realizing inverse design of soft matter.[10,11] Identifying signs of critical behavior is also important when addressing dynamical questions.[12–14]

Classical density functional theory (DFT)[15–17] provides a suitable theoretical framework in which machine learning can be integrated naturally, as was shown in early works,[18–24] for anisotropic particles[25–27] and in a variety of further contexts.[28–32] Bui and Cox have used machine learning to address solvation across length scales,[33] electromechanics,[34] dielectrocapillarity,[35] and ionic fluids.[36] In this paper, we build upon our previous work where density functional learning via a local learning strategy was used in a variety of physical settings,[37–47] including the investigation of hard core correlation effects[37,38] and of interparticle attraction[45,46] in describing gas–liquid phase separation in one-component systems.

We focus on a simple model binary mixture whose bulk phase behavior has been investigated in many simulation and theoretical studies. By contrast, the nature of fluid–fluid interfaces, the accompanying surface tensions, and wetting transitions have been addressed to a much smaller extent, with theories usually employing square-gradient or local density approximations.[48–55] Setting the scene, we note the following: (i) it remains very difficult to progress beyond the naïve mean-field incorporation of attraction within DFT, (ii) predicting bulk phase behavior on the basis of sophisticated integral equation theories remains challenging,[56,57] and (iii) carrying out accurate simulation work at interfaces in mixtures[52,53,58,59] is also challenging and requires systematic understanding of the bulk phase behavior.[52,53,58,60–65]

Here, we adopt a new data-driven perspective to the physics of liquid–liquid phase separation, in which machine learning methods are deeply embedded and are inspired by DFT. In particular, we consider the phase behavior and interfacial structure of a *symmetrical* model binary mixture characterized by Lennard-Jones (LJ) pair potentials $\phi_{ij}(r) = 4\varepsilon_{ij}[(a_{ij}/r)^{12} - (a_{ij}/r)^{6}]$ acting between

particles of species i and j where the species indices $i, j = 1, 2$. We take $a_{11} = a_{22} = a_{12} = a$, i.e., identical diameters for each species, and consider weakened interparticle attraction between species 1 and 2, i.e., $\varepsilon_{11} = \varepsilon_{22} = \varepsilon$ and $\varepsilon_{12} < \varepsilon$. Each potential is truncated at $2.5a$. Such a model has been investigated by several authors. Our choice of parameters was motivated by those in the extensive simulation studies of Wilding *et al.*[52,53,60] who investigated bulk phase behavior and wetting at a particular solid substrate. Their bulk phase diagrams point to the occurrence of what they and later authors term a λ line, which is the line of critical transitions (upper consolute points) between a mixed (binary) fluid and a demixed (binary) fluid. For a range of ε_{12}, the λ line meets the line of two-phase coexistence between the gas (vapor) and the liquid at a critical end point (CEP), occurring at the temperature T_{CEP}. Such behavior is found in real fluid mixtures, type II in the important classification of van Konynenburg and Scott.[2] We choose $\varepsilon_{12} = 0.7\varepsilon$ for which simulation studies[52,53,61] indicate that T_{CEP} lies well-below the gas–liquid critical temperature. This information served as background for our training—see the following—but did not directly influence our choice of parameter space.

To apply the local learning scheme[37–39,44,45] to the LJ mixture, we use grand canonical Monte Carlo simulations (GCMC) to generate training data in the form of species-resolved (one-body) density profiles, $\rho_1(z)$ and $\rho_2(z)$, which are inhomogeneous along a single coordinate z. We consider planar geometry such that the system is translationally invariant in the two perpendicular x and y directions. The simulations are carried out for randomized values of temperature T within the range $0.9 < k_B T/\varepsilon < 2.0$ employing species-dependent, independently randomized forms of the external potentials $V_{\mathrm{ext}}^{(1)}(z)$ and $V_{\mathrm{ext}}^{(2)}(z)$.[37] Then, the species-resolved Euler–Lagrange equations allow one to obtain the one-body direct correlation functions $c_1^{(1)}(z)$ and $c_1^{(2)}(z)$ according to

$$c_1^{(i)}(z) = \ln \rho_i(z) + \beta V_{\mathrm{ext}}^{(i)}(z) - \beta\mu_i, \tag{1}$$

where $i = 1, 2$, inverse temperature is $\beta = 1/(k_B T)$, with Boltzmann constant k_B, and the thermal wavelengths are set to unity. In all simulations, the species-dependent chemical potentials μ_i are set equal, such that $\mu_1 = \mu_2 = \mu$ in Eq. (1), with randomized values of μ chosen uniformly within the range $-7 < \mu/\varepsilon < 4$. The species-resolved external potentials are constructed following the randomization process laid out in Ref. 37. Crucially, the randomization of $V_{\mathrm{ext}}^{(1)}(z)$ and $V_{\mathrm{ext}}^{(2)}(z)$ occurs independently in order to provide enough "contrast" between the two species, i.e., we deliberately avoid $V_{\mathrm{ext}}^{(1)}(z) = V_{\mathrm{ext}}^{(2)}(z)$. This choice ensures we sufficiently probe the relevant density inhomogeneities for the two species.

Having access to the pair of partial density profiles $\rho_1(z)$ and $\rho_2(z)$ together with the corresponding partial one-body direct correlation functions $c_1^{(1)}(z)$ and $c_1^{(2)}(z)$[15–17] obtained via Eq. (1) allows training a neural network to represent the density functional relationship $c_1^{(i)}(z; [\rho_1, \rho_2], T)$; we indicate functional dependence by square brackets. We represent this functional using the local learning scheme,[37–39,44,45] whereby a standard multilayer perceptron outputs both values of $c_1^{(i)}(z; [\rho_1, \rho_2])$, $i = 1, 2$, given as input the discretized partial density profiles $\rho_1(z'), \rho_2(z')$ within a window $|z' - z| < z_w$ around the position z of interest. We choose the spatial cutoff $z_w = 3.5a$ following Ref. 45. The dependence on temperature is captured by thermal training[45–47] and by including the value of T as an additional input node. We note that a single neural network with two output nodes is used to yield values of $c_1^{(i)}(z)$ for both species $i = 1, 2$ simultaneously, which is in contrast to Ref. 36. While no symmetrization regarding the interchange of species is implemented directly in the neural network architecture, we use data augmentation during training and provide samples with flipped species indices as well as flipped on the z axis to benefit from the underlying symmetry. Figure 1 displays a typical choice of external potentials together with density profiles corresponding to a typical choice of thermodynamic parameters.

The trained neural one-body direct correlation functional $c_1^{(i)}(z; [\rho_1, \rho_2], T)$ encapsulates the effects of the interparticle interactions in the fluid mixture, as we will demonstrate. In general, one can make ready and accurate predictions, for arbitrary external potentials, by self-consistent numerical solution of the species-resolved Euler–Lagrange equations,

$$\rho_i(z) = \exp\left[-\beta V_{\mathrm{ext}}^{(i)}(z) + \beta\mu_i + c_1^{(i)}(z; [\rho_1, \rho_2], T)\right], \tag{2}$$

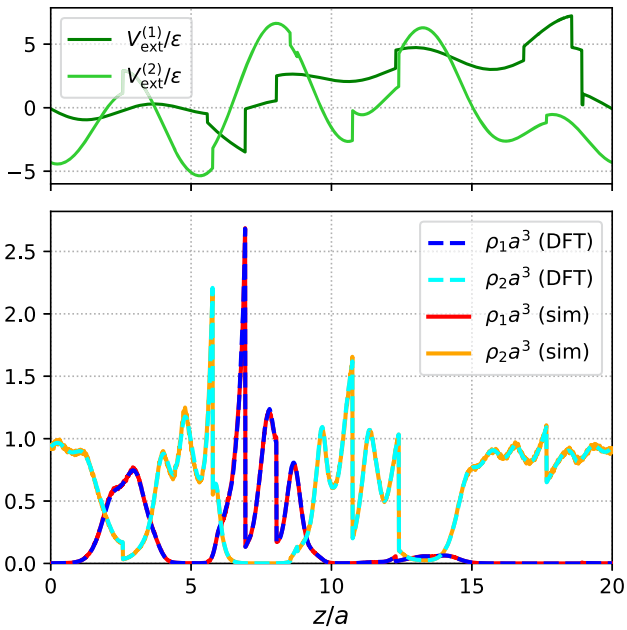

FIG. 1. To exemplify the generation of the training dataset, a specific realization of a randomized inhomogeneous environment is shown. This is characterized by the species-resolved external potentials $V_{\mathrm{ext}}^{(1)}(z)/\varepsilon$ and $V_{\mathrm{ext}}^{(2)}(z)/\varepsilon$ (top panel), chemical potentials $\mu_1/\varepsilon = \mu_2/\varepsilon = 0.237\,599$, and temperature $k_B T/\varepsilon = 1.118\,673$. GCMC simulation results for the partial density profiles $\rho_1(z)$ and $\rho_2(z)$ are used in the local training of the species-resolved one-body direct correlation functional $c_1^{(i)}(z; [\rho_1, \rho_2], T)$, $i = 1, 2$; see the text for details of the neural network. While the training data consist of qualitatively similar profiles, the realization shown was not included in the training set, thereby enabling a direct test of neural network predictions. The self-consistent solution of the Euler–Lagrange Eq. (2) using the trained neural density functional yields results for the partial density profiles (labeled "DFT") that are identical on the scale of the plot to data generated by direct GCMC simulations ("sim") for the specific external potentials; see the bottom panel.

which can be obtained formally from Eq. (1) by exponentiating and identifying the density functional dependence in $c_1^{(i)}(z;[\rho_1,\rho_2],T)$. Equation (2) is solved self-consistently via standard mixed Picard iteration. Predictions for the partial density profiles from Eq. (2) with the neural density functional are highly accurate; see Fig. 1 for a typical inhomogeneous situation, whereby Eq. (2) is solved using prescribed values of $\mu_1 = \mu_2 = \mu$ and T.

We aim to apply the neural density functional to bulk phase coexistence and hence consider situations where both external potentials vanish, $V_{\text{ext}}^{(1)}(z) = V_{\text{ext}}^{(2)}(z) = 0$. For stabilizing coexisting fluid states, we fix the mean value of one partial density via normalization in each iteration step. Note that this determines implicitly the chemical potential $\mu_1 = \mu_2 = \mu$, which is equal for both species due to the employed symmetry. Under appropriate initialization of the Picard iteration procedure to solve the Euler–Lagrange Eq. (2), the theory predicts stable interfacial density profiles, where the partial density profiles crossover within an interfacial region between differing plateau (bulk) values. We find that, depending on the statepoint chosen and the constraints employed within the iteration, all expected types of fluid–fluid coexistence emerge as solutions of Eq. (2). We first display results for $k_BT/\varepsilon = 0.93$ (top and middle panels in Fig. 2), where in addition to the partial density profiles $\rho_1(z)$ and $\rho_2(z)$, we also show the total density $\mathcal{N}(z) = \rho_1(z) + \rho_2(z)$.

At this (low) temperature, we find three distinct interfaces: (i) $\alpha\beta$, where α is a gas and β a liquid with majority component 1, (ii) $\alpha\gamma$, where γ is a liquid with majority component 2, and (iii) $\beta\gamma$, the liquid–liquid interface. Note that the $\alpha\beta$ interface displays an adsorption maximum for the profile of species 2 and that the $\alpha\gamma$ interface (not shown) displays, respecting symmetry, an equivalent maximum for species 1. By contrast, the density profiles of both species are monotonic at the $\beta\gamma$ interface. Such behavior was suggested in early DFT calculations,[48] albeit for a weakly asymmetrical mixture.

The existence of three ($\alpha\beta$, $\alpha\gamma$, and $\beta\gamma$) interfaces for temperature $k_BT/\varepsilon = 0.93$, shown in Fig. 2, implies that this particular statepoint lies on the (fluid) three-phase line of our model. Indeed, reading off the plateau values of the density profiles shown in Fig. 2 yields values for the bulk densities of each species in the coexisting phases. On raising the temperature, we reach a point where the density profiles at the $\beta\gamma$ interface become identical and flat and we associate this with the critical end point T_{CEP}. For higher temperatures, $T > T_{\text{CEP}}$, there is no longer demixing between the two liquid phases and gas (α) coexists with a mixed ($\beta\gamma$) liquid phase. There is a single $\alpha - \beta\gamma$ interface; the bottom panel of Fig. 2 with $k_BT/\varepsilon = 1.00$ provides an example. We return to the bulk phase diagram later but first turn attention to the liquid–liquid ($\beta\gamma$) interfaces and coexistence that we determine at total densities larger than those shown in Fig. 2. In particular, we choose to fix the total bulk density $\rho_1 + \rho_2$ and increase T. The symmetry of our model LJ liquid mixture dictates that the two demixed liquid phases must exhibit a symmetrical Ising-like coexistence curve when expressed in terms of a composition variable $X_1 = \rho_1/(\rho_1 + \rho_2)$, with the upper critical point at $X_1 = 1/2$.

In Fig. 3 (top panel), we plot the coexistence values of X_1 as a function of temperature, while keeping the total bulk density $\rho_1 + \rho_2 = 0.663a^{-3}$ fixed. Recall that $\mu_1 = \mu_2 = \mu$ holds due to

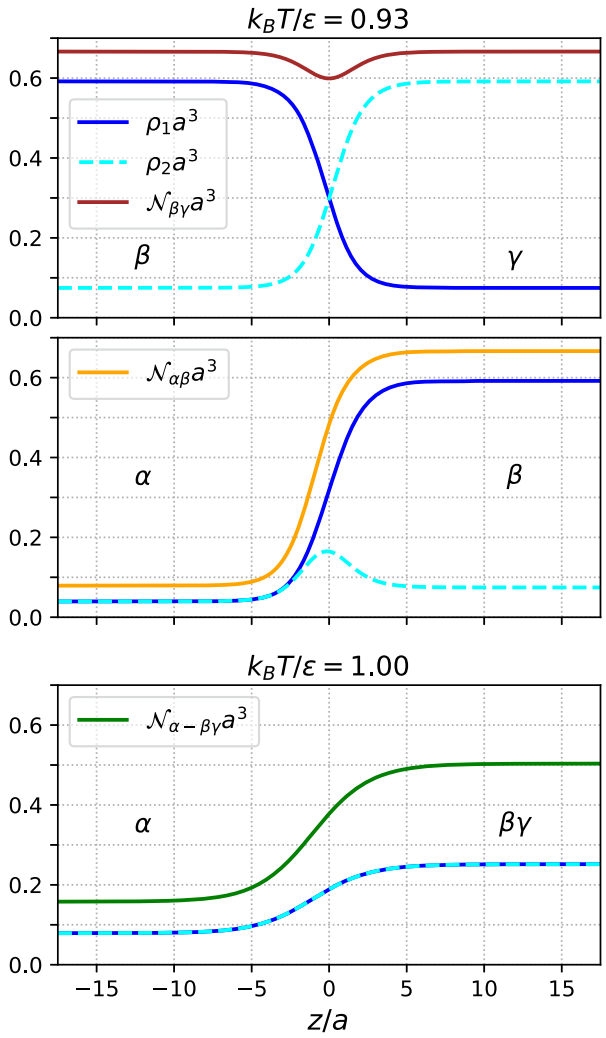

FIG. 2. Density profiles at the different types of fluid–fluid interfaces predicted by the neural DFT: $\beta\gamma$ liquid–liquid (top panel) and $\alpha\beta$ gas-demixed liquid (second panel) at the scaled temperature $k_BT/\varepsilon = 0.93$. Shown are the scaled partial density profiles $\rho_1(z)a^3$ and $\rho_2(z)a^3$, as well as the scaled total density profile $\mathcal{N}(z)a^3 = [\rho_1(z) + \rho_2(z)]a^3$. The $\alpha\gamma$ interface (not shown) is identical to the $\alpha\beta$ interface upon exchanging species 1 and 2. At the increased temperature $k_BT/\varepsilon = 1.0$, the system displays α–$\beta\gamma$ coexistence (bottom panel) between α gas and mixed $\beta\gamma$ liquid with identical partial density profiles, $\rho_1(z) = \rho_2(z)$.

symmetry, but that the value of μ changes, as expected, along the path of constant total density upon varying T, as shown in Fig. 3 (middle panel). The two liquid branches meet at an upper critical temperature T_λ at $X_1 = 1/2$. As an alternative to tracing out the liquid–liquid binodal and determining the merging point of both branches, T_λ can also be identified as the point of vanishing second derivative of the grand potential Ω with respect to composition X_1; see the gray cross in Fig. 3. Automatic differentiation of the neural functional enables this calculation to be performed efficiently,[37] which allows mapping out the line of λ points in the phase diagram

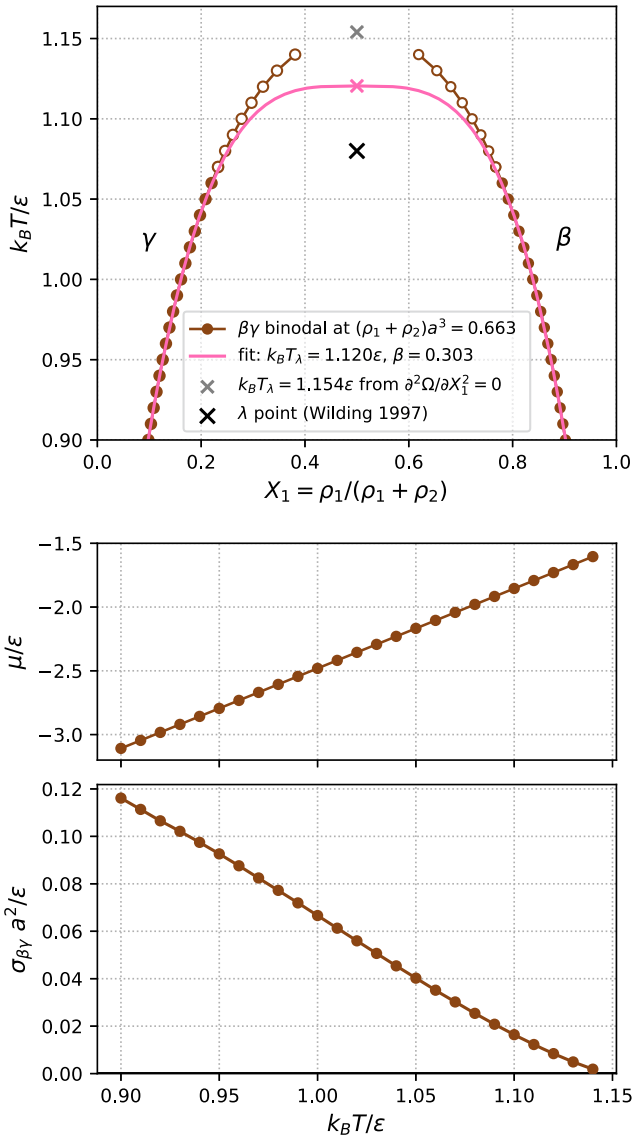

FIG. 3. Top panel: neural density functional results for the bulk $\beta\gamma$ liquid–liquid binodal at fixed total bulk density $(\rho_1+\rho_2)a^3 = 0.663$ shown as a function of bulk composition $X_1 = \rho_1/(\rho_1+\rho_2)$ and scaled temperature k_BT/ε. The results (circles) are obtained from the plateau values of equilibrium interfacial density profiles (see the top panel in Fig. 2). The fit according to Eq. (3) is obtained using only data below and including cutoff temperature $k_BT/\varepsilon = 1.06$ (brown circles), with the resulting numerical values for k_BT_λ/ε and exponent β given in the legend. For comparison, the black cross denotes the λ point obtained from simulation by Wilding.[60] Middle panel: variation of the scaled chemical potential $\mu/\varepsilon = \mu_1/\varepsilon = \mu_2/\varepsilon$ with respect to temperature along the specified path of constant total density. Bottom panel: neural density functional results for the scaled tension $\sigma_{\beta\gamma}a^2/\varepsilon$ of the $\beta\gamma$ interface obtained from functional line integration (4).

at low computational cost. We return to this in Fig. 4, but proceed first with what should be a more accurate estimation of the value T_λ, taking into account the subtleties that arise when evaluating the neural functional close to critical points.[45]

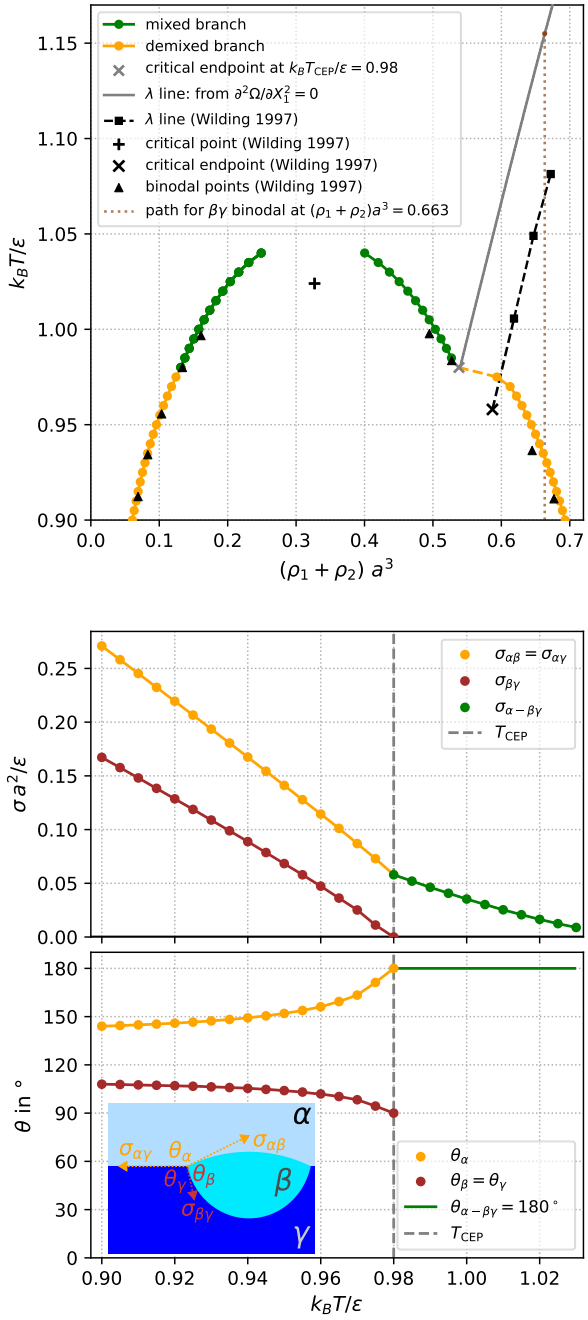

FIG. 4. Top panel: bulk fluid phase diagram of the symmetrical binary Lennard-Jones system as a function of scaled total density $(\rho_1+\rho_2)a^3$ and scaled temperature k_BT/ε together with simulation data of Wilding.[60] Binodals and the λ line are plotted. The vertical dotted red line indicates the path of constant total density for which the liquid–liquid binodal is shown in Fig. 3. Middle panel: scaled interfacial tensions between gas and demixed liquid, $\sigma_{\alpha\beta}a^2/\varepsilon = \sigma_{\alpha\gamma}a^2/\varepsilon$, and between liquid and liquid, $\sigma_{\beta\gamma}a^2/\varepsilon$, for $T < T_{CEP}$, and between the gas and the mixed liquid, $\sigma_{\alpha-\beta\gamma}a^2/\varepsilon$ (green dots), for $T > T_{CEP}$. The dashed vertical line indicates T_{CEP}. Bottom panel: contact angles θ_α and $\theta_\beta = \theta_\gamma$ on the triple phase line, obtained from Eq. (5). The sketch shows the lens of (demixed) liquid β together with the contact angles and tensions.

In particular, we adapt the fitting method used for the gas–liquid binodal in the pure LJ system[45] and use the empirical Ising/lattice gas scaling form for this particular liquid–liquid phase separation,

$$X_1 = \frac{1}{2} \pm b|T^* - T_\lambda^*|^\beta, \tag{3}$$

where $T^* = k_B T/\varepsilon$ is scaled temperature, b is a constant, the critical concentration is $1/2$ per symmetry, and the exponent β should neither be confused with inverse temperature nor with the liquid phase in which species 1 is the majority component. Because of the Ising-like symmetry, there is no need to include a linear contribution in Eq. (3). The three-dimensional Ising value is $\beta = 0.326\,30(22)$,[66] but here the exponent β is treated as a free fit parameter. Following Ref. 45, we exclude data very close to the critical λ point, using only coexisting densities for $k_B T/\varepsilon \leq 1.06$, and find from the fitting $T_\lambda^* = 1.120$ and $\beta = 0.303$ for this particular total density; see Fig. 3. T_λ obtained from the fitting procedure is about 3% lower than the value obtained from direct evaluation of the neural functional by tracing the $\beta\gamma$ binodal, i.e., calculating the merging of coexisting density profiles or, equivalently, from the vanishing of the second-derivative of the grand potential.

Our framework allows us to access interfacial tensions via expressing the excess free energy difference $\Delta F_{\rm exc}$ as a functional line integral,

$$\frac{\beta \Delta F_{\rm exc}}{A} = -\int dz \sum_{i=1,2} \Delta\rho_i(z) \int_0^1 ds\, c_1^{(i)}(z; [\rho_{1,s}, \rho_{2,s}], T), \tag{4}$$

where A is the lateral area of the system and the density profiles $\rho_{1,s}(z)$ and $\rho_{2,s}(z)$ used as functional arguments are taken to be superpositions $\rho_{i,s}(z) = s\rho_i(z) + (1-s)\rho_i$, where ρ_i is the bulk coexistence density for species $i = 1, 2$ and the difference between start and end densities is $\Delta\rho_i(z) = \rho_{i,1}(z) - \rho_{i,0}(z) = \rho_i(z) - \rho_i$. Then, the surface tension is obtained from the excess grand potential $\sigma = (\Omega + pV)/A$, where p is the pressure at coexistence. The results, shown in Fig. 3 (bottom panel), indicate as expected that $\sigma_{\beta\gamma}$ decreases monotonically with temperature and that it vanishes as $T \to T_\lambda$.

We return now to the full phase diagram obtained from considering density profiles such as those shown in Fig. 2. Analysis of the plateau values of all stable fluid interfaces allows us to construct the entire fluid phase diagram, shown in the top panel of Fig. 4, and plotted as a function of the total density $\rho_1 + \rho_2$ and temperature T. We have checked that for $T > T_{\rm CEP}$, the results obtained for coexisting densities are numerically consistent with those obtained via the Maxwell construction based on bulk functional integration.[37] The representation in Fig. 4 makes apparent the density jump at gas–liquid coexistence. Recall that above the CEP, the liquid is in a mixed state; both species have equal concentration. Below the CEP, the liquid is demixed, as discussed above, and the concentration jump (see Fig. 3) is "collapsed" in the representation of Fig. 4. As described above, the λ line is calculated from the locus of vanishing second derivative of the grand potential Ω with respect to composition X_1, readily facilitated via automatic differentiation of the neural functional.[37] While our results for the gas–liquid binodal agree closely with the independent simulation data of Wilding,[60] our λ line displays a small offset, typically about 10% in density, with respect to the corresponding simulation results.

We obtain the surface tensions for gas–liquid coexistence again via Eq. (4), adapted to the respective bulk coexistence conditions. Figure 4 (middle panel) displays results obtained below $T_{\rm CEP}$ for the surface tensions of the gas–liquid interfaces, $\sigma_{\alpha\beta} = \sigma_{\alpha\gamma}$, and for the liquid–liquid interface, $\sigma_{\beta\gamma}$. The latter vanishes at $T_{\rm CEP}$, cf. Fig. 3. For $T > T_{\rm CEP}$, the surface tension refers to the gas–liquid interface, $\sigma_{\alpha-\beta\gamma}$, where the liquid is now in a mixed state.

At triple phase coexistence below $T_{\rm CEP}$, three fluid phases can meet in stable mechanical contact and form a lens of, say, the liquid β phase. The corresponding contact angles θ_α, θ_β, and θ_γ characterize the (macroscopic) shape of the lens and satisfy $\theta_\alpha + \theta_\beta + \theta_\gamma = 2\pi$; see e.g., Ref. 55. Generally, the contact angles are determined by the three surface tensions via the well-known Neumann triangle construction.[55] The symmetry of our LJ mixture dictates that the surface tensions $\sigma_{\alpha\beta} = \sigma_{\alpha\gamma}$, so that the triangle is isosceles and $\theta_\beta = \theta_\gamma$. It follows that

$$\cos\theta_\beta = -\frac{\sigma_{\beta\gamma}}{2\sigma_{\alpha\beta}}. \tag{5}$$

Only the ratio of the respective interfacial tensions is relevant. The form of the liquid lens, as determined by the three tensions, together with results for the contact angles as a function of temperature, are shown in the bottom panel of Fig. 4. Approaching $T_{\rm CEP}$ from below, we find, as expected, $\theta_\beta = \theta_\gamma \to \pi/2$ and $\theta_\alpha \to \pi$.

For our *symmetrical* model, there can be no transition to complete wetting of the $\alpha\gamma$ interface by liquid β for $T < T_{\rm CEP}$: the right-hand side of Eq. (5) can only vanish at $T_{\rm CEP}$. This implies partial wetting, i.e., a finite lens, rather than the intervention of a thick film of phase β, pertains for all $T < T_{\rm CEP}$—an observation pertinent for the general physics of wetting transitions at fluid–fluid interfaces. The latter topic continues to attract considerable attention; see, e.g., Parry and Rascón,[67] Indekeu and Koga,[68] and references therein. Remarks: (i) the consequences for wetting imposed by symmetry of the interparticle potentials were already implicit in Sec. 8.3 of Ref. 55; (ii) breaking the symmetry can lead to first order[49] or critical[67] wetting transitions below $T_{\rm CEP}$; and (iii) determining accurately the behavior of the surface tensions close to $T_{\rm CEP}$ is very difficult within the neural functional framework;[45] similar considerations apply to direct simulation studies.

In conclusion, we have investigated the bulk fluid phase behavior and associated interfacial phenomena in a symmetrical LJ mixture with a specific choice of weakened cross attraction. While imposing symmetry serves conveniently to reduce the parameter space, the model already incorporates a wealth of physics that is challenging to describe within a machine learning context: the lack of *a priori* symmetry breaking is important. A single neural network was used to represent the pair of species-resolved one-body direct correlation functionals simultaneously. This strategy is consistent with the formal generation of $c_1^{(i)}(\mathbf{r}; [\rho_1, \rho_2], T)$ via functional differentiation from a single, underlying, excess free energy functional.

Training the neural functional is based on adapting both the local learning[37] and thermal training[45] schemes that were previously developed for single-component systems. Using these methods directly for the present binary mixture allows one to learn solely on the basis of the available simulation data. We have found that small

artifacts can arise thereby in the predictions of the precise shape and location of the gas–liquid binodal when using the above-mentioned schemes without modification. These artifacts are prevented by including L_2 regularization[69] in the training protocol, which we have hence adopted for the neural functional that was used to generate all numerical results shown in this work. The two different neural models trained with and without L_2 regularization, together with a comparison of the corresponding numerical predictions, are available in Ref. 70. In future work, it would be interesting to investigate physics-informed regularization, e.g., by incorporating exact statistical mechanical sum rules[71] to provide additional constraints that are to be optimized during training.

Working with the trained neural density functional is computationally more efficient than carrying out direct simulations to determine the (bulk) phase diagram. Moreover, we demonstrated that the methodology provides systematic access to subtle interfacial properties. It would be very interesting for simulation experts to test the predictions for surface tensions and contact angles in Fig. 4. Determining these remains a significant challenge for direct simulation work. The benefits of the neural method far outweigh the very moderate computational overhead for creating the training data,[72] which involves standard and cheap simulations of inhomogeneous one-body density profiles of sufficient variability, straightforward to ensure in practice using appropriate random external potentials. Predictions made with the neural functional are numerically robust and agree quantitatively with reference data for statepoints away from criticality. Overcoming limitations close to critical points, where correlation effects on large length scales related to critical fluctuations become relevant, remain to be properly incorporated.

Functional differentiation provides access to the partial two-body direct correlation functions[37,45] and, hence via the Ornstein–Zernike route, to partial bulk and interfacial structure factors which provide further insight into the physics of liquid–liquid phase separation and the nature of the line of upper consolute points (λ line). For example, at points on this line, all three bulk structure factors $S_{ij}(k)$ diverge at wave number $k = 0$ but the isothermal compressibility does not diverge. The results will be presented elsewhere.

It is compelling to apply our methodology to broader types of fluid mixtures. For example, simply changing the cross parameter gives rise to a tricritical point for sufficiently large ε_{12}, and intricate wetting behavior is expected to be found for the asymmetric case, $\varepsilon_{11} \neq \varepsilon_{22}$. These scenarios can all be studied with neural density functionals. We expect our machine learning technique to fare very well with the increased parameter space,[47] provided that sufficient training data can be generated. A chemical engineer might inquire how well we can address realistic (chemical) substances. The applicability of our method clearly hinges upon the availability of reference data and their effective incorporation into the framework of DFT.[73–75] The present paper focuses on the underlying physics of the approach.

The neural density functional is available online, and we recall its universal applicability in planar inhomogeneous situations, cf. Figure 1.

We are grateful to A. O. Parry and N. B. Wilding for valuable conversations and for providing references. Some of the calculations were performed using the emil-cluster of the Bayreuth Center for High Performance Computing funded by the DFG (Deutsche Forschungsgemeinschaft) under Project No. 422127126. This work was supported by the DFG (Deutsche Forschungsgemeinschaft) under Project No. 551294732.

AUTHOR DECLARATIONS

Conflict of Interest

The authors have no conflicts to disclose.

Author Contributions

Silas Robitschko: Data curation (lead); Formal analysis (lead); Investigation (equal); Methodology (equal); Software (lead); Visualization (equal); Writing – review & editing (equal). **Florian Sammüller**: Conceptualization (equal); Data curation (equal); Investigation (supporting); Methodology (equal); Software (supporting); Visualization (equal); Writing – review & editing (equal). **Matthias Schmidt**: Conceptualization (equal); Methodology (equal); Supervision (equal); Writing – original draft (equal); Writing – review & editing (equal). **Robert Evans**: Conceptualization (equal); Methodology (equal); Supervision (equal); Writing – original draft (equal); Writing – review & editing (equal).

DATA AVAILABILITY

The data that support the findings of this study are openly available in https://doi.org/10.5281/zenodo.17188538.[70]

REFERENCES

[1] D. Frenkel and B. Smit, *Understanding Molecular Simulation: From Algorithms to Applications*, 3rd ed. (Academic Press, Amsterdam, 2023).
[2] P. H. van Konynenburg and R. L. Scott, "Critical lines and phase equilibria in binary van der Waals mixtures," Philos. Trans. R. Soc., A **298**, 495–540 (1980).
[3] F. Sciortino, Y. Zhai, S. L. Bore, and F. Paesani, "Constraints on the location of the liquid–liquid critical point in water," Nat. Phys. **21**, 480–485 (2025).
[4] A. J. Archer, B. D. Goddard, D. N. Sibley, J. T. Rawlings, R. Broadhurst, F. F. Ouali, and D. J. Fairhurst, "Experimental and theoretical bulk phase diagram and interfacial tension of ouzo," Soft Matter **20**, 5889–5903 (2024).
[5] D. N. Sibley, B. D. Goddard, F. F. Ouali, D. J. Fairhurst, and A. J. Archer, "Coexisting multiphase and interfacial behavior of ouzo," Phys. Fluids **37**, 042118 (2025).
[6] A. A. Hyman, C. A. Weber, and F. Jülicher, "Liquid-liquid phase separation in biology," Annu. Rev. Cell Dev. Biol. **30**, 39–58 (2014).
[7] J. Arnold, F. Schäfer, A. Edelman, and C. Bruder, "Mapping out phase diagrams with generative classifiers," Phys. Rev. Lett. **132**, 207301 (2024).
[8] E. Bedolla, L. C. Padierna, and R. Castañeda-Priego, "Machine learning for condensed matter physics," J. Phys.: Condens. Matter **33**, 053001 (2021).
[9] V. Chertenkov, E. Burovski, and L. Shchur, "Finite-size analysis in neural network classification of critical phenomena," Phys. Rev. E **108**, L032102 (2023).
[10] M. Dijkstra and E. Luijten, "From predictive modelling to machine learning and reverse engineering of colloidal self-assembly," Nat. Mater. **20**, 762–773 (2021).
[11] G. M. Coli, E. Boattini, L. Filion, and M. Dijkstra, "Inverse design of soft materials via a deep learning–based evolutionary strategy," Sci. Adv. **8**, eabj6731 (2022).
[12] Z. Liu, X. Zhang, X. Ru, T.-T. Gao, J. M. Moore, and G. Yan, "Early predictor for the onset of critical transitions in networked dynamical systems," Phys. Rev. X **14**, 031009 (2024).

[13]B. Harris, L. L. Gollo, and B. D. Fulcher, "Tracking the distance to criticality in systems with unknown noise," Phys. Rev. X **14**, 031021 (2024).
[14]A. Morr and N. Boers, "Detection of approaching critical transitions in natural systems driven by red noise," Phys. Rev. X **14**, 021037 (2024).
[15]R. Evans, "The nature of the liquid-vapour interface and other topics in the statistical mechanics of non-uniform, classical fluids," Adv. Phys. **28**, 143–200 (1979).
[16]R. Evans, "Density functionals in the theory of nonuniform fluids," in *Fundamentals of Inhomogeneous Fluids*, edited by D. Henderson (Marcel Dekker, New York, 1992), Chap. 3, pp. 85–176.
[17]R. Evans, M. Oettel, R. Roth, and G. Kahl, "New developments in classical density functional theory," J. Phys.: Condens. Matter **28**, 240401 (2016).
[18]T. Santos-Silva, P. I. C. Teixeira, C. Anquetil-Deck, and D. J. Cleaver, "Neural-network approach to modeling liquid crystals in complex confinement," Phys. Rev. E **89**, 053316 (2014).
[19]L. Shang-Chun and M. Oettel, "A classical density functional from machine learning and a convolutional neural network," SciPost Phys. **6**, 025 (2019).
[20]S.-C. Lin, G. Martius, and M. Oettel, "Analytical classical density functionals from an equation learning network," J. Chem. Phys. **152**, 021102 (2020).
[21]P. Cats, S. Kuipers, S. de Wind, R. van Damme, G. M. Coli, M. Dijkstra, and R. van Roij, "Machine-learning free-energy functionals using density profiles from simulations," APL Mater. **9**, 031109 (2021).
[22]P. Yatsyshin, S. Kalliadasis, and A. B. Duncan, "Physics-constrained Bayesian inference of state functions in classical density-functional theory," J. Chem. Phys. **156**, 074105 (2022).
[23]X. Fang, M. Gu, and J. Wu, "Reliable emulation of complex functionals by active learning with error control," J. Chem. Phys. **157**, 214109 (2022).
[24]C. Qiao, X. Yu, X. Song, T. Zhao, X. Xu, S. Zhao, and K. E. Gubbins, "Enhancing gas solubility in nanopores: A combined study using classical density functional theory and machine learning," Langmuir **36**, 8527–8536 (2020).
[25]A. Simon, J. Weimar, G. Martius, and M. Oettel, "Machine learning of a density functional for anisotropic patchy particles," J. Chem. Theory Comput. **20**, 1062–1077 (2024).
[26]A. Simon, L. Belloni, D. Borgis, and M. Oettel, "The orientational structure of a model patchy particle fluid: Simulations, integral equations, density functional theory, and machine learning," J. Chem. Phys. **162**, 034503 (2025).
[27]J. Yang, R. Pan, J. Sun, and J. Wu, "High-dimensional operator learning for molecular density functional theory," J. Chem. Theory Comput. **21**, 5905 (2025).
[28]F. Glitsch, J. Weimar, and M. Oettel, "Neural density functional theory in higher dimensions with convolutional layers," Phys. Rev. E **111**, 055305 (2025).
[29]J. Dijkman, M. Dijkstra, R. van Roij, M. Welling, J.-W. van de Meent, and B. Ensing, "Learning neural free-energy functionals with pair-correlation matching," Phys. Rev. Lett. **134**, 056103 (2025).
[30]M. M. Kelley, J. Quinton, K. Fazel, N. Karimitari, C. Sutton, and R. Sundararaman, "Bridging electronic and classical density-functional theory using universal machine-learned functional approximations," J. Chem. Phys. **161**, 144101 (2024).
[31]A. Malpica-Morales, P. Yatsyshin, M. A. Durán-Olivencia, and S. Kalliadasis, "Physics-informed Bayesian inference of external potentials in classical density-functional theory," J. Chem. Phys. **159**, 104109 (2023).
[32]R. Pan, X. Fang, K. Azizzadenesheli, M. Liu-Schiaffini, M. Gu, and J. Wu, "Neural operators for forward and inverse potential-density mappings in classical density functional theory," arXiv:2506.06623 [physics.chem-ph] (2025).
[33]A. T. Bui and S. J. Cox, "A classical density functional theory for solvation across length scales," J. Chem. Phys. **161**, 104103 (2024).
[34]A. T. Bui and S. J. Cox, "A first principles approach to electromechanics in liquids," J. Phys.: Condens. Matter **37**, 285101 (2025).
[35]A. T. Bui and S. J. Cox, "Dielectrocapillarity for exquisite control of fluids," arXiv:2503.09855 [cond-mat.soft] (2025).
[36]A. T. Bui and S. J. Cox, "Learning classical density functionals for ionic fluids," Phys. Rev. Lett. **134**, 148001 (2025).
[37]F. Sammüller, S. Hermann, D. de las Heras, and M. Schmidt, "Neural functional theory for inhomogeneous fluids: Fundamentals and applications," Proc. Natl. Acad. Sci. U. S. A. **120**, e2312484120 (2023).
[38]F. Sammüller, S. Hermann, and M. Schmidt, "Why neural functionals suit statistical mechanics," J. Phys.: Condens. Matter **36**, 243002 (2024).
[39]F. Sammüller, Neural functional theory for inhomogeneous fluids – Tutorial, https://github.com/sfalmo/NeuralDFT-Tutorial.
[40]D. de las Heras, T. Zimmermann, F. Sammüller, S. Hermann, and M. Schmidt, "Perspective: How to overcome dynamical density functional theory," J. Phys.: Condens. Matter **35**, 271501 (2023).
[41]T. Zimmermann, F. Sammüller, S. Hermann, M. Schmidt, and D. de las Heras, "Neural force functional for non-equilibrium many-body colloidal systems," Mach. Learn.: Sci. Technol. **5**, 035062 (2024).
[42]F. Sammüller, S. Robitschko, S. Hermann, and M. Schmidt, "Hyperdensity functional theory of soft matter," Phys. Rev. Lett. **133**, 098201 (2024).
[43]F. Sammüller and M. Schmidt, "Why hyperdensity functionals describe any equilibrium observable," J. Phys.: Condens. Matter **37**, 083001 (2025).
[44]F. Sammüller and M. Schmidt, "Neural density functionals: Local learning and pair-correlation matching," Phys. Rev. E **110**, L032601 (2024).
[45]F. Sammüller, M. Schmidt, and R. Evans, "Neural density functional theory of liquid-gas phase coexistence," Phys. Rev. X **15**, 011013 (2025).
[46]M. Buchanan, "Machine learning predicts liquid–gas transition," Physics **18**, 17 (2025).
[47]S. M. Kampa, F. Sammüller, M. Schmidt, and R. Evans, "Metadensity functional theory for classical fluids: Extracting the pair potential," Phys. Rev. Lett. **134**, 107301 (2025).
[48]M. M. Telo da Gama and R. Evans, "The structure and surface tension of the liquid-vapour interface near the upper critical end point of a binary mixture of Lennard-Jones fluids: I. The two phase region," Mol. Phys. **48**, 229–250 (1983).
[49]M. M. Telo da Gama and R. Evans, "The structure and surface tension of the liquid-vapour interface near the upper critical end point of a binary mixture of Lennard-Jones fluids: II. The three phase region and the Cahn wetting transition," Mol. Phys. **48**, 251–266 (1983).
[50]P. Tarazona, R. Evans, and U. Marini Bettolo Marconi, "Pairwise correlations at a fluid-fluid interface: The influence of a wetting film," Mol. Phys. **54**, 1357–1392 (1985).
[51]I. Hadjiagapiou and R. Evans, "Adsorption from a binary fluid mixture: The composite wetting film at the solid-vapour interface," Mol. Phys. **54**, 383–406 (1985).
[52]F. Schmid and N. B. Wilding, "Wetting of a symmetrical binary fluid mixture on a wall," Phys. Rev. E **63**, 031201 (2001).
[53]N. B. Wilding and F. Schmid, "Wetting of a symmetrical binary fluid mixture on a wall," Comput. Phys. Commun. **147**, 149–153 (2002).
[54]I. Napari, A. Laaksonen, V. Talanquer, and D. W. Oxtoby, "A density functional study of liquid–liquid interfaces in partially miscible systems," J. Chem. Phys. **110**, 5906–5912 (1999).
[55]J. S. Rowlinson and B. Widom, *Molecular Theory of Capillarity* (Dover Publications, Mineola, NY, 2002).
[56]E. Schöll-Paschinger and G. Kahl, "Self-consistent Ornstein–Zernike approximation for a binary symmetric fluid mixture," J. Chem. Phys. **118**, 7414–7424 (2003).
[57]O. Antonevych, F. Forstmann, and E. Diaz-Herrera, "Phase diagram of symmetric binary fluid mixtures: First-order or second-order demixing," Phys. Rev. E **65**, 061504 (2002).
[58]F. J. Martínez-Ruiz, A. I. Moreno-Ventas Bravo, and F. J. Blas, "Liquid-liquid interfacial properties of a symmetrical Lennard-Jones binary mixture," J. Chem. Phys. **143**, 104706 (2015).
[59]S. Roy and F. Höfling, "Critical surface adsorption of confined binary liquids with locally conserved mass and composition," Mol. Phys. **122**, e2391998 (2024).
[60]N. B. Wilding, "Critical end point behavior in a binary fluid mixture," Phys. Rev. E **55**, 6624–6631 (1997).
[61]N. B. Wilding, F. Schmid, and P. Nielaba, "Liquid-vapor phase behavior of a symmetrical binary fluid mixture," Phys. Rev. E **58**, 2201–2212 (1998).
[62]J. Köfinger, G. Kahl, and N. B. Wilding, "Phase behaviour of a symmetrical binary mixture in a field," Europhys. Lett. **75**, 234–240 (2006).
[63]J. Köfinger, N. B. Wilding, and G. Kahl, "Phase behavior of a symmetrical binary fluid mixture," J. Chem. Phys. **125**, 234503 (2006).
[64]S. Roy, S. Dietrich, and F. Höfling, "Structure and dynamics of binary liquid mixtures near their continuous demixing transitions," J. Chem. Phys. **145**, 134505 (2016).

[65]Y. Pathania, D. Chakraborty, and F. Höfling, "Continuous demixing transition of binary liquids: Finite-size scaling from the analysis of sub-systems," Adv. Theory Simul. **4**, 2000235 (2021).
[66]A. M. Ferrenberg, J. Xu, and D. P. Landau, "Pushing the limits of Monte Carlo simulations for the three-dimensional Ising model," Phys. Rev. E **97**, 043301 (2018).
[67]A. O. Parry and C. Rascón, "Wetting, algebraic curves, and conformal invariance," Phys. Rev. Lett. **133**, 238001 (2024).
[68]J. O. Indekeu and K. Koga, "Wetting and nonwetting near a tricritical point," Phys. Rev. Lett. **129**, 224501 (2022).
[69]Using L_2 regularization during training is a standard practice in machine learning which penalizes large values in the neural network parameters. This supports the generation of less complex ("smooth") models, which is particularly suitable for the functional mapping $c_1^{(i)}(\mathbf{r};[\rho_1,\rho_2],T)$.
[70]S. Robitschko (2025). "Learning the bulk and interfacial physics of liquid-liquid phase separation with neural density functionals - Data and Models," Zenodo, Code and models available at: https://github.com/SilasRobitschko/SWNeural and https://doi.org/10.5281/zenodo.17188538
[71]S. Hermann and M. Schmidt, "Noether's theorem in statistical mechanics," Commun. Phys. **4**, 176 (2021).
[72]F. Sammüller and M. Schmidt, "Determining the chemical potential via universal density functional learning," arXiv:2506.15608 [cond-mat.soft] (2025).
[73]C. Klink and J. Gross, "A density functional theory for vapor–liquid interfaces of mixtures using the perturbed-chain polar statistical associating fluid theory equation of state," Ind. Eng. Chem. Res. **53**, 6169–6178 (2014).
[74]P. Rehner, A. Bardow, and J. Gross, "Modeling mixtures with PCP-SAFT: Insights from large-scale parametrization and group-contribution method for binary interaction parameters," Int. J. Thermophys. **44**, 179 (2023).
[75]B. Bursik, N. Karadimitriou, H. Steeb, and J. Gross, "Static contact angles of mixtures: Classical density functional theory and experimental investigation," arXiv:2506.21007 [physics.flu-dyn] (2025).